JGR Solid Earth

RESEARCH ARTICLE
10.1029/2019JB017962

Key Point:
- Our results suggest that surface transient signal can help to detect deep subduction dynamics

Supporting Information:
- Supporting Information S1
- Movie S1
- Movie S2
- Movie S3

Correspondence to:
A. Briaud,
arthur.briaud@uniroma3.it

Citation:
Briaud, A., Agrusta, R., Faccenna, C., Funiciello, F., & van Hunen, J. (2020). Topographic fingerprint of deep mantle subduction. *Journal of Geophysical Research: Solid Earth*, *125*, e2019JB017962. https://doi.org/10.1029/2019JB017962

Received 2 MAY 2019
Accepted 28 DEC 2019
Accepted article online 2 JAN 2020

Topographic Fingerprint of Deep Mantle Subduction

Arthur Briaud[1,2], Roberto Agrusta[2,3], Claudio Faccenna[1,4,5], Francesca Funiciello[1], and Jeroen van Hunen[2]

[1]Laboratory of Experimental Tectonics, Department of Sciences, Roma Tre University, Rome, Italy, [2]Department of Earth Sciences, Durham University, Durham, UK, [3]Laboratoire de Géologie de Lyon, Université de Lyon, École Normale Supérieure de Lyon, Lyon, France, [4]Department of Geological Sciences, Jackson School of Geosciences, The University of Texas at Austin, Austin, TX, USA, [5]Institute for Geophysics, Jackson School of Geosciences, The University of Texas at Austin, Austin, TX, USA

Abstract The dynamic topography links with the mantle structures at various temporal and spatial scales. However, it is still unclear how it relates to the dynamics of subducting lithosphere when plates reach the mantle transition zone and lower mantle. Seismic tomography images show how slab morphologies vary from sinking subvertically into the lower mantle, to lying flat above the upper-lower mantle discontinuity, to thickening in the shallow lower mantle. These slab shapes have been considered to be the result of variable interaction of the slab with the upper-lower mantle discontinuity at ~670 km depth. Previous studies show that periodic deep slab dynamics can explain a variety of enigmatic geological and geophysical observations such as periodic variations of the plate velocities, trench retreat and advance episodes, and the scattered distribution of slab dip angle in the upper mantle. In this study, we use two-dimensional subduction models to investigate the surface topography expression and its evolution during slab transition zone interaction. Our models show that topography does not depend on slab morphology; indeed, the dynamic topography cannot distinguish between a slab sinking straight into the lower mantle and slab stagnation at the upper-lower mantle boundary. However, topographic oscillations are related to episodes of the trench advance and retreat, which in turn are linked to the slab folding behavior at transition zone depths. Our results suggest that the surface transient signal observed by geological studies could help to detect deep subduction dynamics.

1. Introduction

Topography is the product of processes occurring over diverse temporal and spatial scales, and the processes that shape the surface can be considered as the combination of three ingredients: the surface processes, the lithospheric isostatic adjustment, and the deep mantle dynamics. The surface processes are mainly linked to tectonic and geomorphic processes (e.g. Pérez-Peña et al., 2010; Sembroni et al., 2016). Crustal and lithosphere deformation is accommodated by isostatic component, which is stable over long timescales, causing lateral density variations of the crust and the lithosphere, which are balanced by rapid vertical adjustments (e.g. Husson & Ricard, 2004; Kaban et al., 2004; Watts, 1978). Dynamic topography is related to stress acting at base lithosphere due to mantle convection and produce a transient signal on the surface (e.g., Arnould et al., 2018; Forte et al., 1993; Gurnis, 1990; Hager & Richards, 1989; Lithgow-Bertelloni, 1997; Lithgow-Bertelloni & Silver, 1998; Liu & Gurnis, 2010; Mitrovica et al., 1989; Panasyuk & Hager, 2000; Zhong & Gurnis, 1994). The dynamic topography is thus expected to be particularly significant during subduction inducing vigorous mantle flow (e.g. Duretz et al., 2011; Mitrovica et al., 1989; Zhong & Gurnis, 1994). Slab shallowing, for example, is expected to produce down-warping of the upper plate and consequent marine transgression (e.g., Gurnis, 1990; Liu et al., 2008; Mitrovica et al., 1989). Variations in slab dip angle associated to slab folding are correlated with oscillation of surface topography (Cerpa et al., 2014; Cerpa et al., 2015; Guillaume et al., 2009; Martinod et al., 2016), whereas downward tilt of the upper plate toward the subduction trench has been shown to be due to the interaction of the slab with the upper lower mantle discontinuity (Crameri & Lithgow-Bertelloni, 2017; Hager, 1984).

Seismic tomography shows that the cold lithosphere has a wide variability of dips and shapes at both upper and lower mantle depths. In particular, at the base of the upper mantle, slabs appear either sink straight in the lower mantle or lay down horizontally above upper/lower mantle discontinuity (about 670 km) or even deeper around 1,000 km (Fukao & Obayashi, 2013; Ricard et al., 1993; Sigloch & Mihalynuk, 2013; Van Der

10.1029/2019JB017962

Meer et al., 2010). Several studies have highlighted the likely mechanisms that may control this slab variability at transition zone and lower mantle depth, and it has been generally accepted that the viscosity contrast between the upper/lower mantle together with the endothermic ringwoodite to post spinel transition at 670 km depth hampers slabs penetration if subduction is accompanied by trench retreat (Agrusta et al., 2017; Christensen, 1996; Čížková & Bina, 2013; Garel et al., 2014; Kincaid & Olson, 1987; Mao & Zhong, 2018). Moreover, the apparent thickening of some slabs into the lower mantle may be explained by the folding of slabs as soon as they start to interact with the mantle transition zone (MTZ) (Běhounková & Čížková, 2008; Lee & King, 2011; Tosi et al., 2015). Indeed, Sigloch and Mihalynuk (2013) suggest that the thick lower mantle anomalies below North America may be indicators of a remnant slab that piled up almost vertically near the MTZ before breaking and sinking into the lower mantle. Slab buckling and folding may be induced by strong slab pull forces linked to the 410-km discontinuity (i.e., olivine to wadsleyite [ol-wd] transition) and by a strong barrier to slab penetration due to the post-spinel phase transition (Běhounková & Čížková, 2008), by the reduction of the thermal expansivity with depth (Tosi et al., 2015), or by the deformation of young and weak subducting plates (Agrusta et al., 2018; Garel et al., 2014).

Here, we use 2D numerical models to define the large-scale topography evolution of the upper plate during subduction. Our result indicates the deformation of the slab into the transition zone, and its subsequent lower mantle penetration is marked by a specific topography fingerprint that can be used as a proxy of deep mantle slab dynamics.

2. Numerical Approach and Model Setup

2.1. Governing Equations and Model Setup

Single-sided subduction, lithospheric models are calculated using CITCOM code (Moresi & Gumis, 1996; Wang et al., 2015). The code uses the finite element method to solve the system of conservation of mass, momentum, and energy equations for an incompressible fluid under the extended Boussinesq approximation (Christensen & Yuen, 1985), infinite Prandtl number, and without internal heating

$$\nabla \cdot \overline{\mathbf{u}} = 0, \tag{1}$$

$$\nabla\left[\overline{\eta}\left(\nabla\overline{\mathbf{u}} + \nabla\overline{\boldsymbol{u}}^{\boldsymbol{T}}\right)\right] - \nabla\cdot\overline{P} = \overline{\alpha}_z\,\mathrm{Ra}\overline{T} - \mathrm{Ra_c}\sum_{i=1}^{n}\mathrm{Rb_i}\overline{\Gamma}_i, \tag{2}$$

$$\left[1+\sum_{i=1}^{n}\left(\frac{d\overline{\Gamma}_i}{d\overline{z}}\,\overline{\gamma}_i^{\,2}\,\frac{\mathrm{Rb_i}}{\mathrm{Ra}}\,\mathrm{Di}\left(\overline{T}+\overline{T}_s\right)\right)\right]\left(\frac{\delta\overline{T}}{\delta\overline{t}}+\overline{\mathbf{u}}\cdot\nabla\overline{T}\right) = \nabla^2\overline{T} - \left[1+\sum_{i=1}^{n}\left(\frac{d\overline{\Gamma}_i}{d\overline{z}}\,\overline{\gamma}_i\frac{\mathrm{Rb_i}}{\overline{\alpha}_z\,\mathrm{Ra}}\right)\right]\overline{\alpha}_z\,\mathrm{Di}\left(\overline{T}+\overline{T}_s\right)\overline{\mathbf{u}}_z + \frac{\mathrm{Di}}{\mathrm{Ra}}\,\overline{\boldsymbol{\sigma}}\,\dot{\overline{\boldsymbol{\varepsilon}}}, \tag{3}$$

$$\frac{\delta C}{\delta t} + \overline{\mathbf{u}}\cdot\nabla C = 0, \tag{4}$$

where $\overline{\boldsymbol{u}}, \overline{\gamma}_i, \overline{P}, \overline{T}, \overline{T}_s, \overline{t}, \overline{z}, \overline{\alpha}_z, \overline{\boldsymbol{\sigma}}, \dot{\overline{\boldsymbol{\varepsilon}}}$, and $\overline{\eta}$ are the dimensionless (indicated by the upper bar) velocity, Clapeyron slope of *ith* phase transition, pressure, temperature, surface temperature, time, depth, coefficient of thermal expansion, stress, strain rate, and viscosity. The parameters Ra, $\mathrm{Rb_i}$, $\mathrm{Ra_c}$, and Di are the thermal Rayleigh number, the boundary Rayleigh numbers associated with the phase transition, the compositional Rayleigh number, which represents the density variation between the continent and the underlying mantle, and the dissipation number, respectively. They are defined as follows:

$$\mathrm{Ra} = \frac{\alpha_0\,g\,\rho_m\Delta T\,H^3}{\kappa\,\eta_0};\mathrm{Rb_i} = \frac{g\,\Delta\rho_i\,H^3}{\kappa\,\eta_0};\mathrm{Ra_c} = \frac{g(\rho_c-\rho_m)\,H^3}{\kappa\,\eta_0};\mathrm{Di} = \frac{\alpha_0\,\rho_m H}{C_p}. \tag{5}$$

The definition and the values of the parameters in Equation (5) are listed in Table 1.

The thermal expansion coefficient is depth dependent, and it is defined as $\overline{\alpha}_z = \exp(-1.1\overline{z})$ (Tosi et al., 2013). The advection term in the energy equation (Equation (3)) and the composition C (Equation (4)) are solved with the marker-in-cell method (*Gerya* & Yuen, 2003), where markers are advected at each time step by the solid flow and interpolated to the finite element integration points.

Table 1
Model Parameters

Symbol	Parameter	Unit	Value
Global parameters			
H	Box height	km	3,000
ΔT	Potential temperature drop	K	1,350
ρ_c	Continental crust density	kg·m^{-3}	2,700
ρ_m	Mantle reference density	kg·m^{-3}	3,300
g	Gravity	m·s^{-2}	9.8
α_0	Surface thermal expansion	K^{-1}	3×10^{-5}
κ	Thermal diffusivity	m^{-2}·s^{-1}	10^{-6}
η_0	Reference viscosity	Pa·s	10^{20}
C_P	Heat capacity	J·kg^{-1}·K^{-1}	1,250
R	Gas constant	J·mol^{-1}·K^{-1}	8.314
Rheological model parameters			
Diffusion creep			
$A_{upper,lower}$	Pre-exponential upper mantle	Pa·s	1.87×10^{9}
	Pre-exponential lower mantle		2.29×10^{14} to 6.87×10^{15}
E	Activation energy upper mantle	J·mol^{-1}	3×10^{5}
	Activation energy lower mantle		2×10^{5}
V	Activation volume upper mantle	m^{3}·mol^{-1}	5×10^{-6}
	Activation volume lower mantle		1.5×10^{-6}
Byerlee's plastic deformation			
f_c	Friction coefficient	-	0.2
σ_{max}	Maximum yield strength	MPa	300
σ_0	Surface yield strength	MPa	20
Mantle phase transition parameters			
$\gamma_{ol\text{-}wd}$	Clapeyron slope ol-wd transition	MPa·K^{-1}	2.5 to 5
$\gamma_{post\text{-}spinel}$	Clapeyron slope wd/rd-ps transition	MPa·K^{-1}	−0.5 to −3
$z_{ol\text{-}wd}$	ol-wd transition equilibrium depth	km	410
$z_{post\text{-}spinel}$	Post-spinel transition equilibrium depth	km	670
$d_{ol\text{-}wd}$	ol-wd transition width	km	20
$d_{post\text{-}spinel}$	Post-spinel transition width	km	20
$T_{ol\text{-}wd}$	ol-wd transition potential temperature	K	1,423
$T_{post\text{-}spinel}$	Post-spinel transition potential temperature	K	1,423
$\Delta\rho_{ol\text{-}wd}$	ol-wd transition density contrast	kg·m^{-3}	250
$\Delta\rho_{post\text{-}spinel}$	Post-spinel transition density contrast	kg·m^{-3}	350

Mantle phase transitions are included in the models using a harmonic phase function (Agrusta et al., 2014). The relative fraction of the heavier phase is described by the phase function Γ, varying from 0 to 1 with respect to pressure and temperature, as follows:

$$\Gamma_i = 0.5\left[1+\sin\left[\pi\frac{\overline{z}-\overline{z}_i-\overline{\gamma}_i\left[\overline{T}-\overline{T}_i\right]}{\overline{d}_i}\right]\right], \tag{6}$$

where $\overline{d}_i$ is the vertical width of the transition i, $\overline{z}_i$ and $\overline{T}_i$ are the depth and the temperature of the phase transitions at equilibrium conditions (Table 1).

The rheological model is assumed to be a combination of a diffusion creep and a pseudo brittle Byerlee rheology (Agrusta et al., 2017). The effective viscosity is thus calculated from the viscosity of individual mechanisms:

$$\eta_{eff} = \min\left(\eta_{diff}, \eta_{byer}\right) \tag{7}$$

with

$$\eta_{diff} = A_{upper,lower}\exp\left(\frac{E_{upper,lower}+PV_{upper,lower}}{RT}\right), \tag{8}$$

and

10.1029/2019JB017962

$$\eta_{\mathrm{byer}} = \frac{\min(\sigma_0 + \mathrm{f_c P}, \sigma_{\max})}{\dot{\varepsilon}_{\mathrm{II}}}. \tag{9}$$

The subscripts upper and lower refer to the upper and lower mantle, respectively (Equation (8)). The others meaning for the parameters are shown in Table 1. For numerical stability, we consider a maximum viscosity of 10^{24} Pa·s.

To define the effective long-wavelength surface topography, we need to evaluate the vertical stress ($\overline{\sigma}_{zz}$) at the surface, which is done using the consistent boundary flux method proposed by Zhong et al. (1993). This method has been proven to be accurate to study long wavelength topography (larger than 1,000 km) (Crameri et al., 2012; Zhong et al., 1996).

The surface normal stress can be translated into an effective surface topography using the density contrast between lithosphere and the surface media (i.e., water for the oceanic part and air for the continental part) using (Turcotte & Schubert, 2002).

$$\mathrm{H_{surf}}(\mathrm{x}, \mathrm{z} = 0) = \frac{\overline{\sigma}_{zz}(\mathrm{x}, \mathrm{z} = 0)\ \eta_0 \frac{\kappa}{\mathrm{H}^2}}{\Delta\rho\ \mathrm{g}}, \tag{10}$$

where H_{surf} is the surface topography, $\overline{\sigma}_{zz}$ is nondimensional normal stress at the surface, $\Delta\rho$ the density contrast between lithospheres and the media (e.g., water or air) (Table 1). We calibrate the surface topography against the present-day average depth of the mid-ocean ridges (MOR) about 2.9 km depth.

In this study, we consider the dynamic component of the topography as the nonisostatic part, which can be related to the mantle flow. To obtain the dynamic component, we remove the isostatic component from the total topography (Equation (10)).

$$\mathrm{H_{dyn}}\ (\mathrm{x}, \mathrm{z} = 0) = \mathrm{H_{surf}}\ (\mathrm{x}, \mathrm{z} = 0) - \left(\mathrm{Iso_{subd}} + \mathrm{Iso_{upper}}\right), \tag{11}$$

where $\mathrm{Iso_{subd}}$ is the isostatic component due to the vertical stress of the subducting plate:

$$\mathrm{Iso_{subd}} = \int_0^{\mathrm{Z}} \mathrm{g}\ \rho_{\mathrm{m}}\ \alpha_{\mathrm{z}} \mathrm{T(z)}\ \mathrm{dz} / (\Delta\rho_{\mathrm{w}}\ \mathrm{g}), \tag{12}$$

whereas $\mathrm{Iso_{upper}}$ is the isostatic component of the upper plate, obtained by vertical stress due to the thermal and compositional part:

$$\mathrm{Iso_{upper}} = \frac{\int_0^{\mathrm{Z}} (\mathrm{g}\ \rho_{\mathrm{m}}\ \alpha_{\mathrm{z}} \mathrm{T(z)} + \mathrm{g\ C}\ \Delta\rho_{\mathrm{cc}}) \mathrm{dz}}{\Delta\rho_{\mathrm{air}} \mathrm{g}}. \tag{13}$$

Z is the integration depth by assuming a compensation level at 300 km depth, $\Delta\rho_{\mathrm{w}}$ is the density contrast between mantle and water ($\Delta\rho_{\mathrm{w}} = \rho_{\mathrm{m}} - 1000$), and $\Delta\rho_{\mathrm{air}}$ for mantle and air ($\Delta\rho_{\mathrm{air}} = \rho_{\mathrm{m}}$).

The size of the numerical domain is 9,000 km wide and 3,000 km deep (Figure 1b). The rectangular nonuniform grid contains 2,880 × 472 elements where the element size varies from 2.5 to 7.5 km. The highest resolution grid ($2.5 \times 2.5\ \mathrm{km}^2$) is localized vertically from 0 to 210 km depth and horizontally between −5250 to 900 km. The mechanical boundary conditions are free slip on all boundaries; hence, the flow is driven only by internal buoyancy forces. The use of free-slip surface boundary appropriately simulates the large-scale (long-wavelength; $>10^3$ km) surface, dynamic, and isostatic topography. However, this method fails to predict the short-wavelength ($<10^3$ km) topography variation as well as the topography resulting from the viscous plate bending (Crameri et al., 2012). The surface free-slip boundary is thus suitable to investigate the large-scale topography evolution of the upper plate. The thermal boundary conditions are 273 K at the surface and 2,773 K at the bottom. On the right-hand side, a MOR profile has been imposed, whereas a zero-heat flux has been imposed on the left-hand side (Figure 1b). The temperature initial condition represents a subducting plate extended from the MOR, which is located at x = −4,500 km, to the trench situated at x = 0 km, with a given age at the trench following the half space cooling model (Turcotte & Schubert, 2002). To avoid subduction initiation complications, an initial slab is present down to 200 km depth with a bending radius of

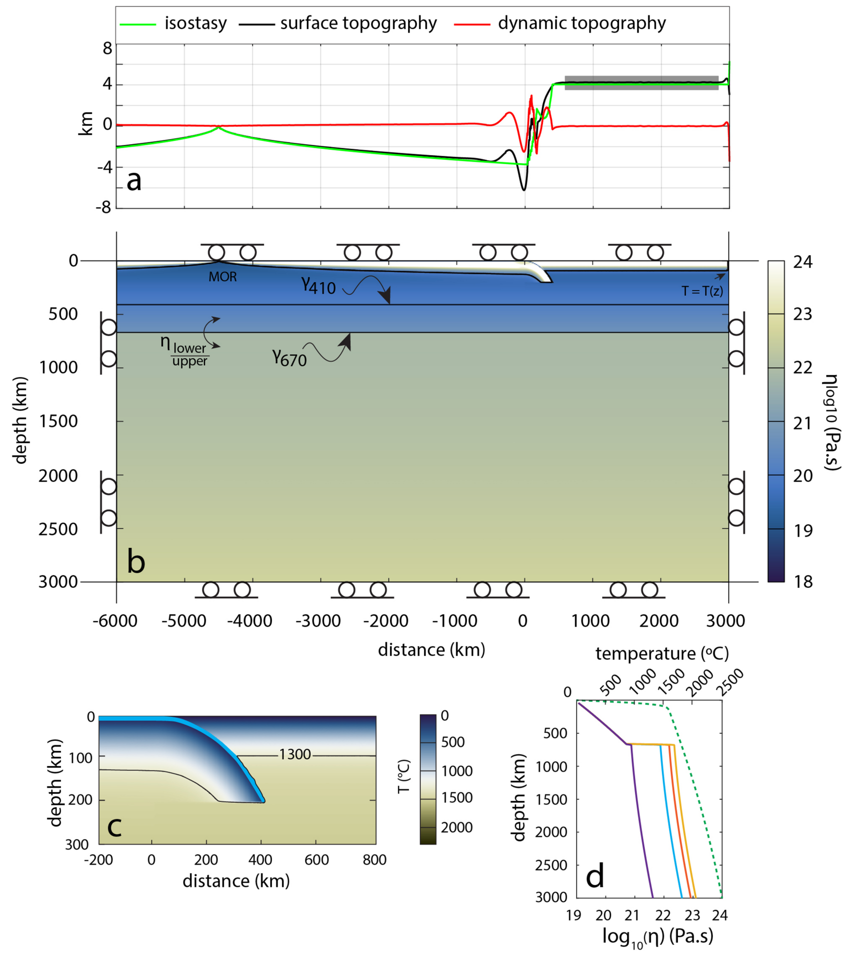

Figure 1. (a) Surface topography (km) in black, with the isostatic and dynamic components in green and red, respectively, for the model domain at $t = 0$ Ma. The grey area corresponds to the measured mean topography (long-wavelength) of the upper plate. (b) Sketch of the model domain at $t = 0$ Ma of a subducting lithosphere with an initial age at the trench of 100 Ma. The background color indicates the viscosity, while the two horizontal black lines (γ_{410} and γ_{670}) represent the equilibrium position of the phase boundaries of olivine-wadsleyite at 410 km depth and the post-spinel transition at 670 km depth. The mid oceanic ridges of the subducting plate is also indicated. $\eta_{\mathrm{upper/lower}}$ indicates the upper/lower mantle viscosity increases. Little rollers on the box sides represent the free slip boundary conditions. (c) Zoom-in on the subduction system. Background color corresponds to the initial temperature conditions. Thick light-blue layer represents the weak layer that decouples the plates. Black solid line represents the 1300°C isotherm. (d) Viscosity (solid lines) and temperature (dashed line) mid oceanic ridge profiles used in this study.

500 km (Figure 1c). The upper plate extends from the right side to the trench, with a constant, initial thermal thickness of about 100 km. A continental crust is present on the upper plate with a thickness of 30 km with a density (ρ_c) of 2,700 kg/m^3. On top of the subducting plate, a 7.5-km thick low viscosity layer of 10^{20} Pa·s is presented down to 200 km depth in order to facilitate the decoupling between the plates (Figure 1c).

2.2. Investigated Parameters

The aim of this work is to investigate the impact of the slab-upper/lower mantle discontinuity interaction on the surface topography. A combination between mantle (i.e., viscosities and phase transformations) and slab properties (i.e., strength and buoyancy) determines the slab behavior at the MTZ (Agrusta et al., 2017; Christensen, 1996; Garel et al., 2014). We systematically vary these parameters.

Two olivine phase transitions are assumed at 410 km depth (the ol-wd (γ_{410})) and at 670 km depth (rg-post-spinel (γ_{670})). We investigate a Clapeyron slope range of ol-wd from +2.5to +5.0 MPa/K, and of post-spinel from −3.0 to −0.5 MPa/K (Faccenda & Dal Zilio, 2017; Katsura & Ito, 1989; Litasov &

Table 2
List of Models with Their Input Variables: Phase Transition Clapeyron Slopes, Lower Mantle Viscosity Prefactor, and the Initial Age of the Plate at the Trench (A_{plate})

Model number	γ_{410} (MPa/K)	γ_{670} (MPa/K)	A_{lower} (Pa s)	A_{plate} (Ma)	t_{670} (Ma)	W_{slab} (km)	Z_{slab} (km)	Category
0	0	0	2.29×10^{14}	100	6.0	126	2,271	1
1	+2.5	−0.5	2.29×10^{15}	100	6.0	168	1,628	2
2	+2.5	−1.0	2.29×10^{15}	100	6.0	211	1,574	2
3	+2.5	−1.5	2.29×10^{15}	100	6.1	256	1,500	2
4	+2.5	−2.0	2.29×10^{15}	100	6.0	1,446	1,111	2
4c	+2.5	−2.0	6.87×10^{15}	100	6.0	1,387	923	2
4g	+2.5	−2.0	2.29×10^{15}	150	5.8	1,502	1,187	2
5	+2.5	−2.5	2.29×10^{15}	100	6.0	1,368	1,042	2
6	+2.5	−3.0	2.29×10^{15}	100	6.0	843	931	2
7	+3.0	−1.5	2.29×10^{15}	100	6.0	266	1,252	2
8	+3.0	−2.0	2.29×10^{15}	100	6.0	1,275	1,088	2
9	+3.5	−3.0	2.29×10^{15}	100	6.0	646	884	3
10	+4.0	−0.5	2.29×10^{15}	100	6.0	354	1,236	1
11a	+4.0	−2.0	2.29×10^{14}	100	6.0	248	1,642	1
11b	+4.0	−2.0	2.29×10^{15}	100	6.0	578	1,679	3
12	+4.0	−2.5	2.29×10^{15}	100	6.0	612	1,433	3
13	+4.0	−3.0	2.29×10^{15}	100	6.0	639	908	3
14	+5.0	−0.5	2.29×10^{15}	100	6.0	369	1,590	3
14e	+5.0	−0.5	2.29×10^{15}	50	6.2	356	1,401	3
14f	+5.0	−0.5	2.29×10^{15}	150	5.9	341	1,770	3
15	+5.0	−1.0	2.29×10^{15}	100	6.1	432	1,644	3
15c	+5.0	−1.0	6.87×10^{15}	100	6.0	526	1,260	3
16	+5.0	−1.5	2.29×10^{15}	100	6.0	476	1,606	3
17a	+5.0	−2.0	2.29×10^{15}	100	6.0	526	1,260	3
17c	+5.0	−2.0	6.87×10^{15}	100	6.1	627	1,135	3
17f	+5.0	−2.0	2.29×10^{15}	150	5.7	560	1,668	3
18	+5.0	−2.5	2.29×10^{15}	100	6.0	587	1,221	3
19a	+5.0	−3.0	2.29×10^{14}	100	6.0	167	1,650	1
19b	+5.0	−3.0	2.29×10^{15}	100	6.0	861	1,832	4
19c	+5.0	−3.0	4.58×10^{15}	100	6.1	1,011	1,472	4
19d	+5.0	−3.0	6.87×10^{15}	100	6.1	1,406	1,213	4
19e	+5.0	−3.0	2.29×10^{15}	25	6.4	570	1,966	4
19f	+5.0	−3.0	2.29×10^{15}	50	6.3	703	1,950	4
19g	+5.0	−3.0	2.29×10^{15}	150	5.8	905	1,934	4

Note. Output variables including: the maximal values of slab length (W_{slab}) and depth (Z_{slab}), the time to reach the 670-km discontinuity (t_{670}) and the category in which each model fits

Ohtani, 2007). The density increases for a mantle composed of 100 wt.% of olivine associated with the phase changes are $\Delta\rho_{410} = 250$ kg/m^3 and $\Delta\rho_{670} = 350$ kg/m^3 for γ_{410} and γ_{670}, respectively (e.g., *Faccenda & Zilio,* 2017; Xu et al., 2008). The averaged upper mantle (averaged between 0 and 670 km depth) viscosity is set to be about 10^{20} Pa·s at mantle temperature. The averaged viscosity of the lower mantle (averaged between 670 and 3,000 km depth) is within a range of 10^{21} to 5×10^{22} Pa·s (Čížková et al., 2012*;* Forte et al., 2002). The initial subducting plate age (i.e., A_{plate}), regulating the slab strength and buoyancy, is varied between 25 and 150 Myr (Table 2). To determine the trench motion during the subduction evolution, we track the trench position (with the initial location at x = 0 km) and its trench velocity (V_t = dXt/dt, positive when the trench moves in the direction of the upper plate). We consider the convergence velocity, defined as $V_{conv} = V_{subd} - V_t$, (with V_{subd} the subducting plate velocity) as a proxy to the slab pull force. For the topographic investigations, we observe throughout our models, sharp variations along of the surface topography. These topographic variations are due to the sharp transition in density between the continental crust and the ocean boundary once the upper plate moves toward the subducting one. To avoid these artifacts, we average surface topography (Equations (11)–(13)) only in the central part of the upper plate, between 800 and 2,200 km from the trench, far away from sharp density variations. Our study then focuses on the large-scale topographic variation of the upper plate (H_{surf}, H_{dyn}). We also measure the dynamic topography rate (Dyn$_{rate}$ = dH$_{dyn}$/dt).

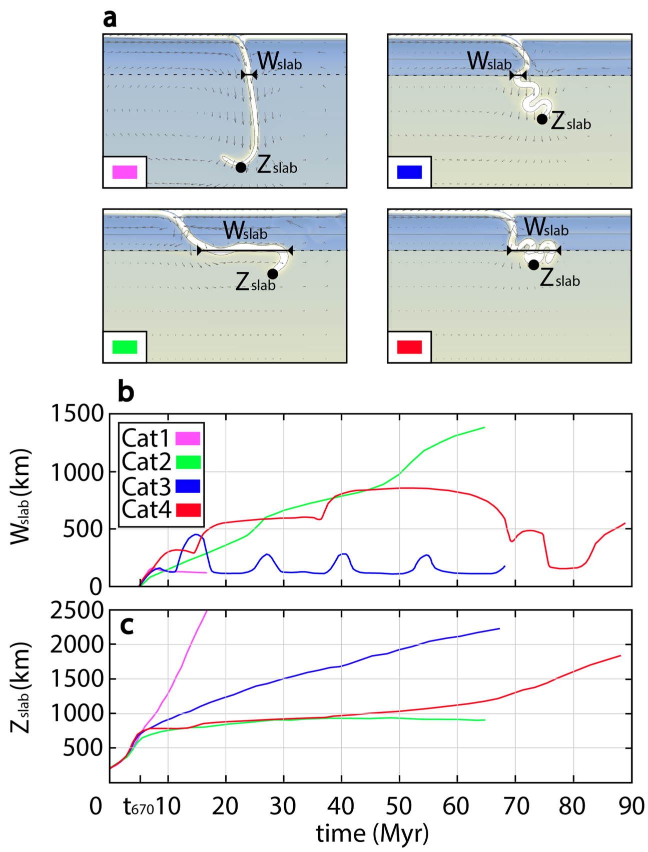

Figure 2. (a) Snapshots of four slab-MTZ interaction modes. (b and c) the time series of the width of the slabs at 670 km (W_{slab}) and slab tip depth (Z_{slab}) for the four cases in (a): (Cat1) category 1, undisturbed slab; (Cat2) category 2, flat slab; (Cat3) category 3, folding slab; (Cat4) category 4, buckling slab and avalanche.

In order to discriminate between different slab behaviors and morphologies, we define two diagnostic measured quantities. The following quantities are evaluated starting from the time the slab reaches 670 km depth (t_{670}), which roughly indicates the time when the slab begins to interact with the upper/lower mantle discontinuity. We measure the width of the slab in the transition zone (W_{slab}) and the maximum slab depth (Z_{slab}) over time (Figure 2a). Those measurements will help us to separate our models into different slab categories. A slab that sinks straight into the lower mantle will display a relatively constant W_{slab}, close to the initial thickness of the subducting plate, and will display an increase of Z_{slab} through time (category 1, Figure 2). A slab that stagnates in the transition zone will show a nearly linear increase of the W_{slab} and a relatively constant (Z_{slab}) (category 2, Figure 2). A slab folding while passing through the MTZ will show oscillations of W_{slab}, and a constant increase of Z_{slab} (category 3, Figure 2). Finally, a slab that will buckle and stagnate for a while in the transition zone, before sinks in the lower mantle, will show an increase of W_{slab} together with an almost constant Z_{slab} (similar to the category 2), during the period of stagnation and buckling, followed by a decrease of W_{slab} and increases of Z_{slab}, for the period of lower mantle sab sinking (category 4, Figure 2). For the example of category 4 shown in Figure 2 the lower mantle sinking occurs at ~60 Myr. W_{slab}, Z_{slab}, and t_{670} are used to define the two dimensionless values t_{fold} and D. t_{fold} is defined as follows:

$$t_{\mathrm{fold}} = \frac{t_{slab}}{t_{670}}, \tag{14}$$

where t_{slab} corresponds to the time needed by the slab to stagnate, and it is the time during which $(W_{\mathrm{slab}} - \langle W_{\mathrm{slab}} \rangle) > 0$ is satisfied, with $\langle W_{\mathrm{slab}} \rangle$ the arithmetic average of W_{slab} in time. t_{fold} indicates thus how much slab material it trapped in the transition zone and for how long.

The second parameter D is the ratio between the rate at which the slab accumulates in the MTZ, and the rate at which the slab sinks in the lower mantle ($D = (\mathrm{d}W_{\mathrm{slab}}/\mathrm{dt})/(\mathrm{d}Z_{\mathrm{slab}}/\mathrm{dt})$).

$$D = \frac{W_{\mathrm{slab}}(t_{\mathrm{end}}) - W_{\mathrm{slab}}(t_{670})}{Z_{\mathrm{slab}}(t_{\mathrm{end}}) - Z_{\mathrm{slab}}(t_{670})}, \tag{15}$$

with t_{end}, the final time of the simulations. D is similar to the parameter defined by Agrusta et al. (2018), and it indicates whether the slab is more prone to sink in the lower mantle or to get trapped in the MTZ. A slab that does not accumulate into the MTZ will have both t_{fold} and D less than 1. On the contrary, these variable will be larger than 1 for a hypothetical slab that will be trapped or interacting for longer time into MTZ.

3. Results

We performed 33 simulations (Table 2) of self-consistent single-sided 2D subduction with the aim to study the expression of the slab dynamics on the surface. In this section, we first describe a reference model of a slab sinking straight into the lower mantle in a simplified setup that does not include mantle phase transitions, and presents a relatively weak lower mantle (with an averaged viscosity of 10^{21} Pa·s) (Table 2). Next, we systematically modify the reference model by changing the strength of the ol-wd and rg-to-post-spinel transitions (γ_{410}; γ_{670}), the prefactor term for the lower mantle viscosity (A_{lower}), and the initial age of the subducting plate (A_{plate}).

In order to describe the deep slab evolution and the corresponding surface expression, we describe the evolution of the model during three distinct phases (e.g., Funiciello et al., 2003), corresponding to three states of slab sinking in the mantle. The first phase corresponds to the interval in which the slab sinks through the upper mantle and lasts until the slab reaches the 670 km depth discontinuity at the t_{670}. The second phase

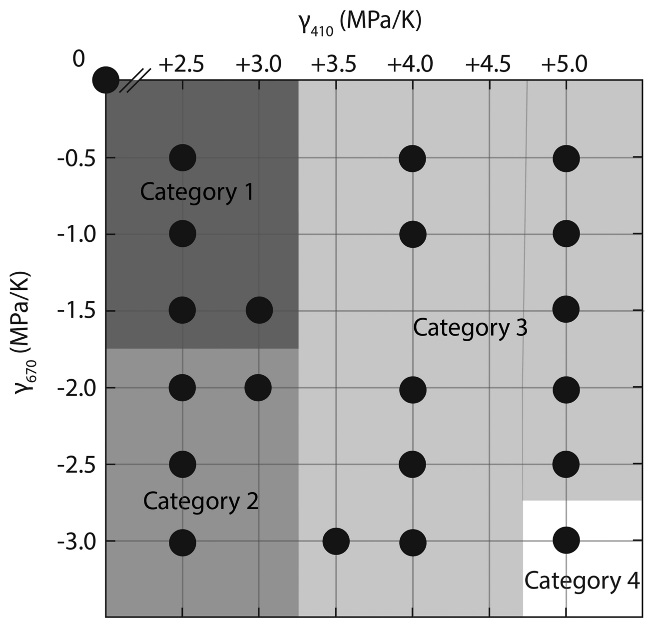

Figure 3. Regime diagram plotting γ_{410} against γ_{670} at either fixed lower mantle viscosity ($A_{lower} = 2.29 \times 10^{15}$ Pa·s) and $A_{plate} = 100$ Ma. Each circle corresponds to a model. Shaded areas corresponds to slab categories: undisturbed slab (category 1), flat slab (category 2), folding slab (category 3), and buckling slab and avalanche (category 4). These areas derive from Figure S2 (supplementary materials that define interaction modes).

occurs during the slab interaction with the upper/lower mantle boundary at 670 km depth when the slab tip depth is stagnating between 670 and 1,000 km depths. The third phase is after slab interaction with the 670 km depth discontinuity when the slab propagate deeper into the lower mantle (Figure 2).

3.1. Reference Model

Previous models have shown that both a weak lower mantle viscosity and a weak mantle endothermic transition (γ_{670}) facilitate slab penetration in the lower mantle (e.g., Goes et al., 2017). Hence, our reference model is characterized by the absence of mantle phase transitions and a relatively weak lower mantle, with an initial subducting plate of 100 Myr (Table 2, model 0; Figure S1 in the supporting information).

During the first phase, the slab sinks freely into the upper mantle until it reaches the base of the upper mantle (Figure S1). The dynamic topography profile remains flat around 0 km without significant lateral variations. During this phase, the convergence velocity (V_{conv}) accelerates from 2 cm/yr to ~5 cm/yr, suggesting an increase in the slab pull force (Figure S1d). At the surface, the trench advances with velocity (V_t) from 4 cm/yr to 2.5 cm/yr (Figure S1f). The topography of the upper plate during this phase remains roughly constant through time, with an averaged elevation (H_{surf}) of 1 km above the sea level with a negligible averaged dynamic component ($H_{dyn} = 0$ km) (Figures S1c and S1e).

After penetrating into the lower mantle, the slab shows a subvertical and linear morphology with a folded tip edge due to the slight increasing lower mantle viscosity (Figure S1b). Yet the dynamic profile along the upper plate remains stable and close to 0 km elevation (Figure S1a). During the slab descent, the V_{conv} increases up to ~10 cm/yr (Figure S1d), while V_t suggests trench advance (Figure S1f). The large-scale surface topography of the upper plate decreases through time, until reaches about 800 m above the seal level at end of the simulations (t_{end}) (Figure S1c). The same trend is observed on the dynamic topography that shows a slow subsidence of 200 m over 7 Myr (Figure S1e).

3.2. Slab Dynamics Categories

The subduction behavior at depth varies due to changes in the following geodynamical parameters with respect to the reference model: A_{plate}, γ_{410}, γ_{670}, and lower mantle viscosity (hereafter indicated by the prefactor A_{lower}) (Table 2). To categorize slab interaction modes depending on the mantle and plate properties, we draw a diagram based on the output variables t_{fold} and D (Figure S2). The models fall in four main categories:

- (Category 1, "undisturbed slab") for $D < 1$ and $t_{fold} < 1$, the slab penetrates almost undisturbed in the lower mantle (similar to the reference model).
- (Category 2, "flat slab") for $D > 1$ and $t_{fold} > 1$, the slab does not penetrate in the lower mantle.
- (Category 3, "folding slab") for $D < 1$ and $1 < t_{fold} < 6$, the slab penetrates in the lower mantle, with folding episodes.
- (Category 4 "buckling slab and avalanche") for $D < 1$ and $t_{fold} > 6$, the slab, before to sink in the lower mantle, it gets trapped in MTZ while folding.

We delineate t_{fold}≈6 as an arbitrary choice. Indeed, we observe throughout our models that t_{fold}≈6 is the limit between category 3 and category 4.

A regime diagram summarizing how the relative behavior of slabs changes with phase transition strengths at the 410 and 670 km depth is shown in Figure 3. Subducting plate age and lower mantle viscosity seem to give a weak contribution to cluster the slab categories, and we will describe their influence on the next sections. There are quite tight ranges of plausible conditions over which undisturbed slabs (category 1), flattening

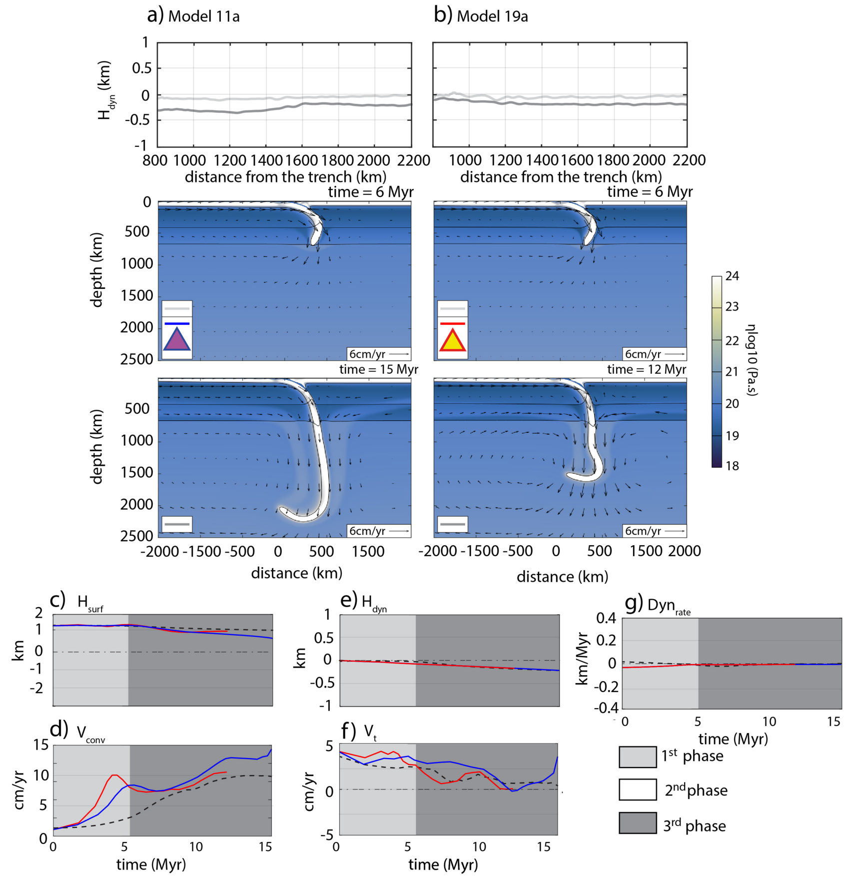

Figure 4. (a and b) Selected time steps in the evolution of the models 11a and 19a (Table 2). Top: dynamic topography profiles. Bottom: zoom-in of the slab morphology. The colors represent the viscosity and the arrow the velocity field. The grey solid line contour is the 1300°C isotherm, while the solid black lines correspond to the mantle phase transitions. Box in the bottom left corner shows the symbol that refers to the plot in Figure S2. The dark and light grey lines indicate the dynamic topography top plots. Time series of the surface topography (c), convergence velocity (d), dynamic topography (e), trench velocity (f), and the dynamic rate of the upper plate (g) of the current models. Dotted black lines are the reference model (Figure S1).

slabs (category 2), and buckling and flushing slabs (category 4) are expected. In contrast, there is a quite wide range over which the folding slab behavior exist (category 3).

3.3. Undisturbed Slab (Category 1)

This undisturbed sinking category includes slabs that neither fold nor accumulate into the MTZ, and their morphologies remain similar to the reference model, displaying a subvertical morphology extended from the surface to lower mantle (Figure 4, Movie S1). We found that the simulations in this category are obtained with the lowest lower mantle viscosity (viscosity with prefactor $A_{\mathrm{lower}} < 2.29 \times 10^{15}$ Pa·s) (Figure 4; Table 2, models 0, 10, 11a, and 19a). As expected, a weak lower mantle does not provide enough resisting force to make the slabs stagnate into the upper mantle that agrees with previous studies (e.g. Agrusta et al., 2017; Mao & Zhong, 2018). The general evolution of those slabs morphology as well as dynamic topographies profile (Figures 4a and 4b) is similar to the reference model in which the effect of phase transitions was not included, and the only difference is the convergence velocity (V_{conv}), since that the presence of the ol-wd mantle phase transition enhances the slab pull (Figure 4d). The trench shows an advancing trend and the topography a weak subsidence (Figures 4c, 4e–4g).

3.4. Flat Slab (Category 2)

Slabs belonging to this category stagnate into the transition zone (Figure 5, Movie S2), and this slab dynamics is promoted by a viscous lower mantle (viscosity prefactor of $A_{\mathrm{lower}} \geq 2.29 \times 10^{15}$ Pa·s) (Table 2;

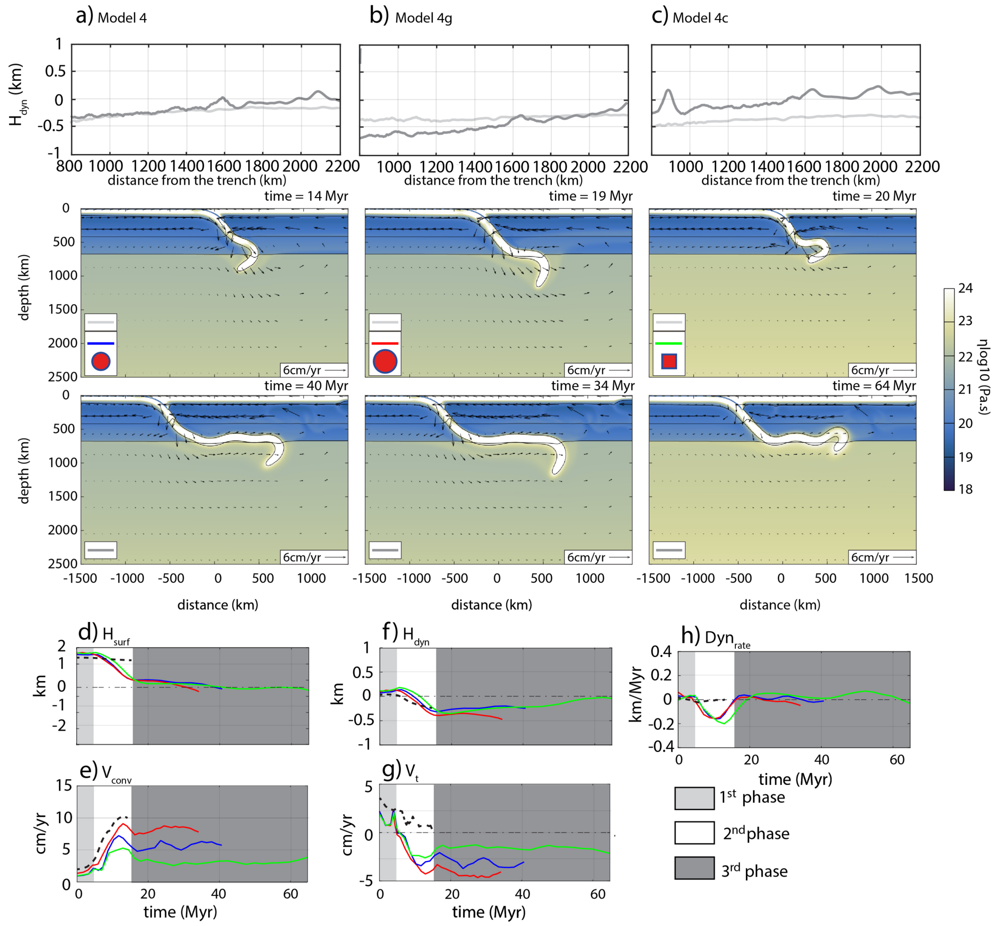

Figure 5. (a, b, and c) Selected time steps in the evolution of the models 4, 4g, and 4c (Table 2). Top: zoom-in on dynamic topography space and time domain. Bottom: zoom-in of the slab morphology. The color represents the viscosity and the arrows the velocity field. The black solid line contour is the 1300°C isotherm. Box in the bottom left corner shows the symbol that refers to the regime diagram in Figure S2. The dark and light grey symbols indicate the dynamic topography top plots. Time series of the surface topography (d), convergence velocity (e), dynamic topography (f), trench velocity (g), and the dynamic rate of the upper plate (h) of the current models. Dotted black lines are the reference model (Figure S1).

Figure 5), and by weak exothermic phase transition ($\gamma_{410} < +3.5$ MPa/K) combined with a strong endothermic one ($\gamma_{670} < -2$ MPa/K (Table 2; Figure 5).

To study the evolution of this slab category, we selected three simulations characterized by similar mantle phase transitions of ol-wd and post-spinel ($\gamma_{410} = +2.5$ MPa/K and $\gamma_{670} = -2$ MPa/K) and different lower mantle viscosities and initial subducting plate ages. These models are shown in Figure 5: model 4 with A_{lower} of 2.29×10^{15} Pa·s and A_{plate} of 100 Myr; model 4g with an older A_{plate} of 150 Myr and the same lower mantle viscosity of the model 4; and the model 4c with A_{lower} of 6.87×10^{15} Pa·s, while the A_{plate} is the same as for model 4 (Table 2).

For each of the three simulations, the first phase where the slab freely falls in the upper mantle lasts about 6 Myr. The dynamic topography profile remains almost flat similar to the profile observed during the same phase for the reference model (Movie S2). The trench advances with V_t of ~1 cm/yr, while V_{conv} speeds up gradually, about 3 cm/yr (Figures 5e and 5g).

After reaching the upper-lower mantle discontinuity, the slab tip folds and deforms into the MTZ (second phase). We observe that, as soon as the slab starts rolling back, a large-scale tilt toward the trench occurs for all models (Figures 5a–5c, top), similar to results in Crameri and Lithgow-Bertelloni (2017) and

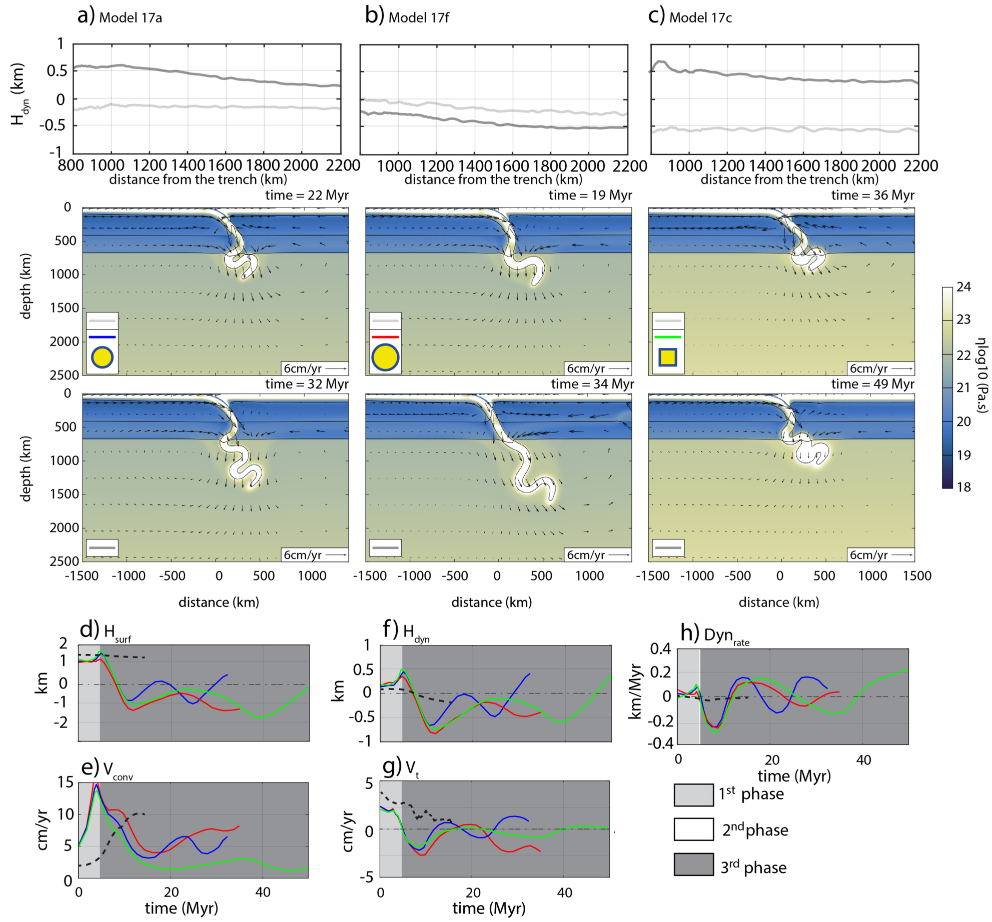

Figure 6. (a, b, and c) Selected time steps in the evolution of the models 17a, 17f, and 17c (Table 2). Top: zoom-in on dynamic topography space and time domain. Bottom: zoom-in of the slab morphology. The color represents the viscosity and the arrow the velocity field. The black solid line contour is the 1300 °C isotherm. Box in the bottom left corner shows the symbol that refers to the regime diagram in Figure S2. The dark and light grey symbols indicate the dynamic topography top plots. Time series of the surface topography (d), convergence velocity (e), dynamic topography (f), trench velocity (g), and the dynamic rate of the upper plate (h) of the current models. Dotted black lines are the reference model (Figure S1).

Mitrovica et al. (1989). The trench starts to retreat with the highest velocity for the oldest plate and the slowest for the models with the more viscous lower mantle. These velocity differences are also observed for the convergence velocity, indicating an increase of the resisting force to the slab sinking in the lower mantle from the more viscous lower mantle and an increase of the driving force from the oldest plate (Figures 5e and 5g). The topographic signals (H_{surf}; H_{dyn}) decrease abruptly for all models as soon as the slabs fold and retreat, with an intensity that does not depend by the slab or lower mantle properties. Along with the tilting, the mean topographies H_{surf} and H_{dyn} show a decrease of about 0.8 and 0.3 km, respectively (Figures 5d, 5f, and 5h).

The third phase is characterized by the deflection and stagnation of the slabs at the base of the upper mantle. Despite similarities between slab morphologies, slabs evolve differently depending on the mantle and slab properties. The younger slab shows undulations of the slab leading edge at the base of the upper mantle, whereas the older slab does not exhibit such deformation (Figures 6a–6c, bottom). Along with the young slab undulations in the MTZ, oscillations are observed in V_{t} (Figures 5a and 5g). The amplitude of V_{t} during trench retreat motion depends on the slab strength: a younger slab increases the amplitude of the trench oscillation, whereas an old slab and/or more viscous lower mantle dampens the undulation of the slab trailing edge into the MTZ, which in turn, drive less oscillations in V_{t}.

The topography (H_{surf}; H_{dyn}), after having reached its minimum at the end of the second phase, remains almost constant for the less viscous lower mantle and the young plate cases, whereas a rise of H_{dyn} is observed for the more viscous lower mantle (Figure 5f). This high dynamic topography elevation is due to the mantle return flow restricted to the upper mantle (Figures 5c and 5f). The topographic profile still keeps its tilted shape (Figures 5a–5c, top).

3.5. Folding Slab (Category 3)

Category 3 (Figure 6) involves simulations that primarily have a strong ol-wd phase transition, combined with relatively strong post-spinel transition and a high lower mantle viscosity (Table 2). Indeed, it is known that strong a ol-wd phase transition (high γ_{410}) increases the sinking velocity of the slab, while both a strong post-spinel phase transition (very negative γ_{670}) and a strong lower mantle hamper slab penetration and may facilitate slab lateral undulation and slab folding behavior (Běhounková & Čížková, 2008; Tosi et al., 2015). This slab behavior is obtained for a strong ol-wd (γ_{410}) transition combined with a moderate post-spinel ($\gamma_{670} < -2$ MPa/K) transition, while the lower mantle viscosity needs a prefactor $A_{lower} > 2.29 \times 10^{15}$ Pa·s (Table 2). To better understand the evolution of these slab transition zone interactions, we look at models with similar values of ol-wd ($\gamma_{410} = +5$ MPa/K) and post-spinel ($\gamma_{670} = -2$ MPa/K) transitions, and we vary the A_{plate} from 100 to 150 Ma and the A_{lower} viscosity prefactor from 2.29×10^{15} Pa·s to 6.87×10^{15} Pa·s (Table 2). Figure 6 shows model 17a, characterized by a A_{plate} of 100 Myr and a A_{lower} of 2.29×10^{15} Pa·s, model 17f, with a A_{plate} of 150 Myr and the same A_{lower}, and model 17c with A_{plate} of 100 Myr and the A_{lower} of 6.87×10^{15} Pa·s (Table 2). Regardless of the transition zone and lower mantle properties, the behavior during the first phase for models in category 3 is comparable to the reference model, and again, the dynamic topography shows a flat profile for the three models. However, we notice that the magnitude of V_{conv} is up to 15 cm/yr, higher than for the previous categories due to the high strength of ol-wd (γ_{410}), which enhances the slab pull force (Figure 6e).

After reaching the base of the upper mantle, the folding slabs propagate directly into the lower mantle. Indeed, due to the weak resisting forces associated with a relatively weak endothermic phase transition, slabs pass easily across the transition zone (Figures 6a–6c). At first view, this behavior looks like the simple, undisturbed sinking slab (category 1). However, due to the strong slab pull force linked to the strength of the ol-wd transition, the slabs fold in the transition zone. Also, the lower mantle affects the behavior of the folding slab. Indeed, the slab does not penetrate easily into the lower mantle, and as a result, narrow folds are generated in the transition zone (Figure 6c, bottom). We observe a dynamic tilting of the upper plate toward the trench once slabs start to retreat. In contrast, if the slab folds and the trench advances, it induces an opposite tilt of the upper plate (Figures 6a–6c, top).

The convergent and trench velocities show oscillation in time (Figures 6e and 6g). The model with $A_{plate} = 150$ Myr shows a period of about 20 Myr, whereas the younger subducting plate shows a period of about 15 Myr. The period of the model with stronger A_{lower} is about 30 Ma. The amplitudes of V_{conv} and V_t are not affected by A_{plate} and remain higher by about 2 cm/yr than the stronger lower mantle viscosity case (Figures 6c, 6e, and 6g).

These variations in velocities correspond to periods of trenches advance and retreat (Figures 6e and 6g). These oscillations with similar periods are also found in the topographic evolutions, which show highs and lows in H_{surf} and H_{dyn} (Figures 6d and 6f). These topographic features follow the trench velocity peaks in time with a delay of ~4 Myr for a weak A_{lower} and A_{plate} values of 100 and 150 Myr (Figures 6a, 6b, 6f, and 6g), whereas models with a strong A_{lower} show a delay of ~7 Myr (Figures 6c, 6d, and 6g). During trench advance, the slab bends toward the upper plate (Figures 6b, top, 6a and 6c, bottom), and as a result, topographic uplift occurs, as shown by the peak in dynamic topographic rate Dyn_{rate} (Figure 6h). In contrast, when the trench retreats, H_{surf} and H_{dyn} decreases, resulting in a minimal Dyn_{rate} (Figure 6h). The amplitude of dynamic topography H_{dyn} varies as function of A_{plate}, where a younger subducting plate induces more topographic amplitude about of 0.2 km (Figure 6f). The amplitude of H_{dyn} for stronger lower mantle viscosities (Figures 6c and 6f) remains similar to what is measured for models with a weaker lower mantle viscosity (Figures 6a and 6f).

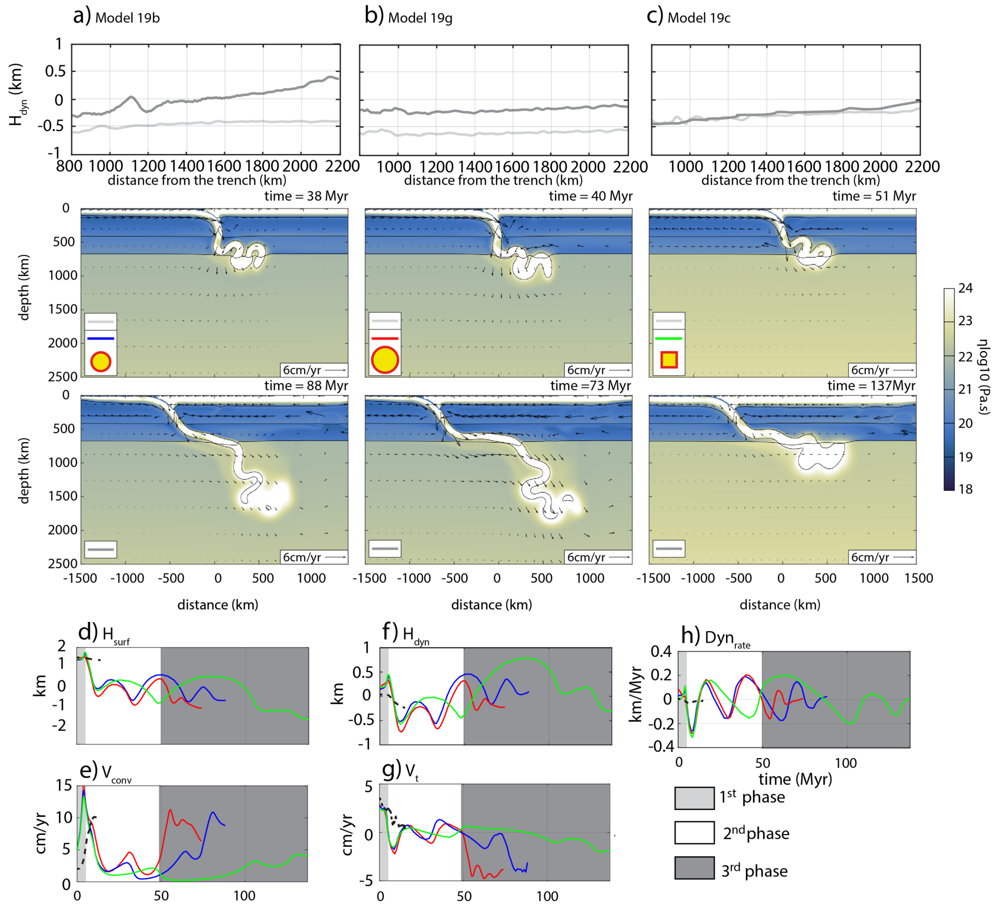

Figure 7. (a, b, and c) Selected time steps in the evolution of the models 19b, 19g, and 19c (Table 2). Top: zoom-in on dynamic topography space and time domain. Bottom: zoom-in of the slab morphology. The color represents the viscosity and the arrow the velocity field. The black solid line contour is the 1300°C isotherm. Box in the bottom left corner shows the symbol that refers to the regime diagram in Figure S2. The dark and light grey symbols indicate the dynamic topography top plots. Time series of the surface topography (d), convergence velocity (e), dynamic topography (f), trench velocity (g), and the dynamic rate of the upper plate (h) of the current models. Dotted black lines are the reference model (Figure S1).

3.6. Buckling Slab and Avalanche (Category 4)

Category 4 differs from the category 3 by showing a long period of slab folding in the MTZ, followed by a slab avalanche behavior into the lower mantle. This is obtained with a strong γ_{670} (Table 2 and Movie S3). To study the evolution of this slab category, we use a model similar to the one used in category 3 but with $\gamma_{670} = -3$ MPa/K (Figures 7a–7c).

As before, we modify the lower mantle viscosity and the A_{plate}. Model 19b has an A_{plate} value of 100 Myr and an A_{lower} value of 2.29×10^{15} Pa·s, whereas model 19b has an older A_{plate} value of about 150 Myr. For model 19c, we increase the A_{lower} at 6.87×10^{15} Pa·s, while we keep the same A_{plate} as in model 19b (Table 2). The first phase lasts 6 Ma (Figure 7). The overall evolution of these models during the journey of the slab into the upper mantle is comparable to what has been described for the category 3.

For the second phase, the creation of folds is mirrored by fluctuations of V_{conv} and V_{t}. When V_{conv} increases, the slab rolls back and the trench retreats. By contrast, when V_{conv} decreases, the slab bends toward the upper plate, and the trench advances (Figures 7a–7c, 7e, and 7g). The amplitude and period of velocities are similar to those recorded in the category 3. The periods are about 30 and 15 Ma for the models with a stronger and weaker lower mantle viscosity, respectively (Figures 7e and 7g). The amplitudes in V_{t} are not affected by A_{plate} and remain higher by about 1 cm/yr than the stronger lower mantle viscosity case (Figures 7c and 7g). Indeed, strong A_{lower} decreases the velocities, because strong A_{lower} decreases the vigor of the convection. Following the V_t oscillation in time, the dynamic topography profiles are similar to those for category 3, episodically experiencing a dynamic tilting of the upper plate toward and away from the trench with respect to the slab folding dynamics and trench movement (Movie S3).

The mean topographic measurements (H_{surf} and H_{dyn}) increase and decrease depending on the slab folding in the transition zone (Figures 7a–7c and 7f). The H_{dyn} amplitudes and periods are also similar to what was recorded in the category 3, with the difference that in these cases the slabs pile up in the transition zone rather than in the lower mantle.

When the slab material that accumulates into the transition zone starts to flush down into the lower mantle (third phase) (Figures 7a–7c, bottom), the dynamic topographic profiles show a sudden high, followed by an abrupt dynamic subsidence of the upper plate (Figures 7a–7c, top). We observe a sharp increase in V_t and V_{conv} for the models with a weak A_{lower} (Figures 7a–7c, 7e, and 7g). On the contrary, model with strong A_{lower} prevents the slab from penetrating into the lower mantle and induces a slow increase in V_t (Figures 7c and 7g). For models 19b and 19g, V_t and V_{conv} increase with up to 5 cm/yr and ~10 cm/yr, respectively (Figures 7a, 7b, 7e, and 7g). Such acceleration is explained by an increase of the slab sinking force, due to the reduced effect of the post-spinel (γ_{670}) resisting force after the slab penetration. In contrast, model 19c shows smaller amplitude in V_t and V_{conv} about 1 and 3 cm/yr, respectively (Figures 7c, 7e, and 7g). Strong lower mantle viscosity hampers the slab sinking into the lower mantle, which, in turn, drives slow trench retreat (Figures 7c and 7g). The velocities (V_{conv} and V_t) show oscillation periods of about 30 and 50 Ma for models with weak A_{lower} and strong A_{lower}, respectively (Figures 7e and 7g). Linked to these new kinematics, H_{surf}, H_{dyn}, and Dyn_{rate} (Figures 7d, 7f, and 7h) show long periods of increasing and decreasing induced by the slab avalanches where the periods are similar to what is recorded in V_t and V_{conv} (Figures 7a–7c, 7e, and 7g). The amplitudes differ according to the geodynamical variables (A_{lower} and A_{plate}). Varying A_{plate} does not change the amplitude of H_{dyn}, which remains about 1.1 km. In contrast, stronger lower mantle viscosity increases the H_{dyn} amplitude by about 0.6 km more than weaker lower mantle (Figure 7f).

After a "slab avalanche," the trench retreats, and we observe a tilting of dynamic topography profile toward the trench. This typical dynamic topography profiles resemble those for the flat slab behavior (category 2). However, there are variations between modes. The steepest tilt is recorded for the weak A_{lower} in combination with $A_{plate} = 100$ Myr, whereas neither old plates nor a viscous lower mantle provides steep tilting of the upper plate (Figures 7b and 7c).

3.7. Sensitivity of the Dynamic Topography with Respect to Deep Slabs Dynamics

To summarize the findings of our parametric study, Figures 8a and 8c show the relationships between the time needed by slabs to fold (i.e., t_{fold}) versus the mean dynamic topography period and the maximum dynamic topographic rate, whereas the maximum thickness of the slab into the transition zone against the maximal dynamic topography amplitude is shown in Figure 8b.

The dynamic topographic period is measured by taking the duration between peaks and averaging these distance. For the amplitudes of the dynamic topography (H_{dyn}) and its rate (Dyn_{rate}), we take their maximum values in time after the first slab/MTZ interactions (i.e., t_{670}).

The dynamic topographic period depends on the ability of the slab to sink into the lower mantle. For the weakest lower mantle viscosity, slabs sink faster into the lower mantle than they do for a more viscous lower mantle case. We observe a relationship between the time spent by the slab in the MTZ (t_{fold}) and the dynamic topographic period. Stronger lower mantle viscosity results in the slab being trapped into the MTZ, which, in turn, increases the dynamic period. In other words, this specific surface fingerprint highlights the fact that the mantle flow is slower for strong mantle viscosity, which in turn, drives a longer dynamic period. On the contrary, the weakest lower mantle viscosity provides less resisting force to slab-mantle-induced flow. The mantle vigor is therefore more efficient, providing a shorter period in dynamic topography (category 1, Figure 8a)

A viscous lower mantle combined with a strong ol-wd transition (i.e., $\gamma_{410} > +3.5$ MPa/K), and a relatively weak post-spinel transition (i.e., $\gamma_{670} > -3.0$ MPa/K) reduces the dynamic period. The age of the subducting plate does not induce significant changes in the period for categories 1, 3, and 4, whereas an old plate decreases the period for category 2.

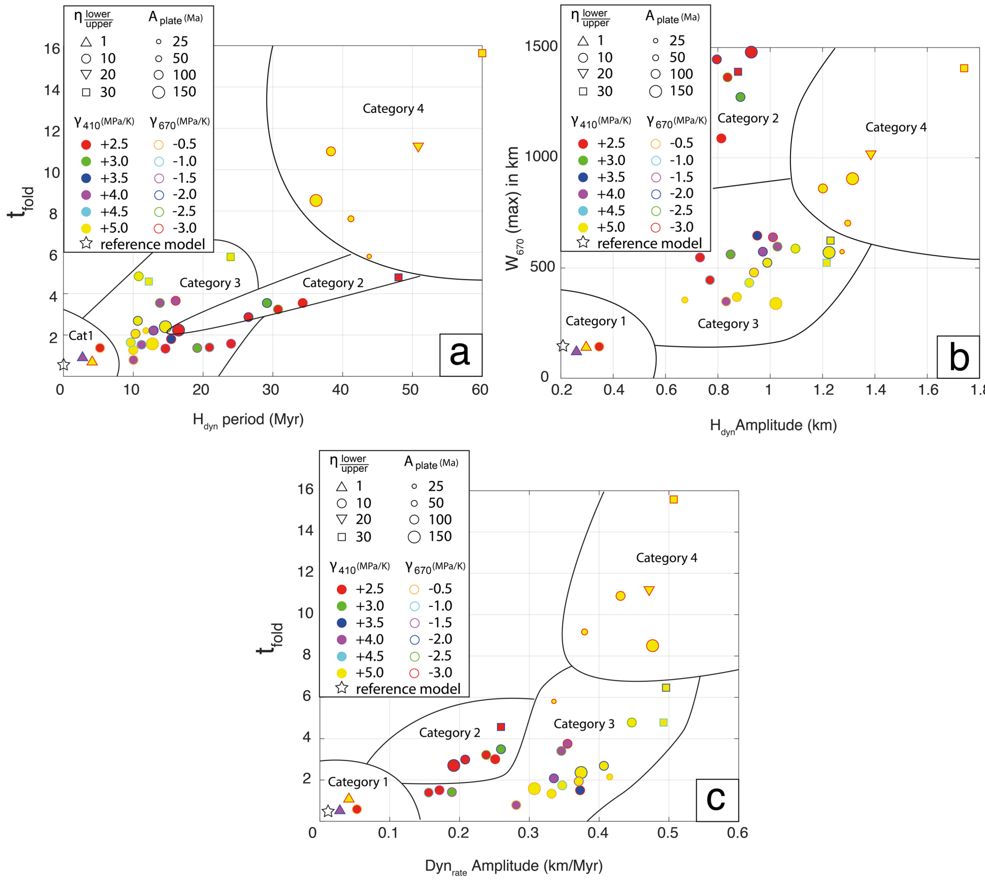

Figure 8. (a) Diagram plotting t_{fold} against the mean dynamic topographic period (H_{dyn}). (b) Diagram plotting the slab thickness in the MTZ (W_{slab} (max)/W_{slab} (t = 0)) versus the dynamic topography amplitude (H_{dyn}). (c) Diagram plotting t_{fold} over the maximum dynamic topography rate ($\mathrm{Dyn}_{\mathrm{rate}}$). As indicated in the legend box, the shape of the symbols represents the lower mantle viscosity. The size of the symbols represents the initial subducting plate age (A_{plate}). The color of the symbols represents the strength of ol-wd transition (γ_{410}). The color of the edges of the symbols represents the strength of post-spinel transition (γ_{670}). Black lines delineate the slab categories areas: straight slab (category 1), flat slab (category 2), folding slab (category 3), and folding slab and avalanche (category 4).

For the dynamic amplitude and its rate, we observe a linear trend between categories 1, 3, and 4 (Figures 8b and 8c). Again, the amplitude increase depends on the viscosity of the lower mantle. A stronger lower mantle together with a large strength of the ol-wd transition (i.e., $\gamma_{410} > +3.5$ MPa/K) and a weak post-spinel one (i.e., $\gamma_{670} < -3.0$ MPa/K) leads to the highest amplitudes in dynamic topography and its rate (Figures 8b and 8c). The slabs from category 2 stand out from the relationship between the maximal width of the slab (W_{670}) and the dynamic amplitude. These models have similar dynamic topography amplitudes, around 900 m (Figure 8b).

The dynamic topographic rate ($\mathrm{Dyn}_{\mathrm{rate}}$) amplitudes are less than ~0.25 km/Myr for both categories 1 and 2. This indicates that neither undisturbed slab (category 1) nor flat slab (category 2) behavior in the MTZ influence the large-scale topography of the upper plate significantly (Figure 8c). On the contrary, categories 3 and 4 show a wide range of dynamic topography rates from ~0.15 to ~0.5 km/Myr. Those values indicate that the folding slab behavior strongly affects the topography of the upper plate. The strong resisting force to slab penetration linked to A_{lower} and γ_{670} drives the highest $\mathrm{Dyn}_{\mathrm{rate}}$ amplitude.

4. Discussion

This study presents 2D self-consistent numerical models showing how the evolution of the slab during its journey into the mantle is represented by the dynamic topography of the overriding plate. The characteristic dynamic topographic signal strongly depends on the slab dynamics at depth. We find that, for each of the

10.1029/2019JB017962

categories presented in Section 3, the slabs behave differently, leading to a different, diagnostic surface expression.

In the category 1, the weak resistance to slab penetration enables vertical slab sinking into the lower mantle. This behavior generates a large-scale return flow producing efficient slab suction (Faccenna et al., 2013). Therefore, the trench does not retreat but instead shows a slight advancing motion. The dynamic topography slightly decreases over time when the slab sinks below the upper lower mantle discontinuity. Indeed, undisturbed sinking slabs into the lower mantle lead to the creation of a much larger convection cell below the upper plate. As a result, the dynamic topography of the upper plate is progressively reduced by the downward mantle flow generated by the sinking slab at depth.

For category 2 slabs, once the slab reaches the 670-km discontinuity, a "slab pull" type dynamics (Faccenna et al., 2013) is observed. At the surface, the dynamic topography is dragged down, and a tilt toward the trench is observed when the slab starts to interact with the upper/lower mantle discontinuity. Both the dynamic topographic low and the topographic tilt remain stationary during slab flattening in the MTZ, due to the steady trench retreat state.

For category 3, episodic fold formation at depth occurs when the slab interacts with the transition zone. This behavior is recurrent in all our models with a strong γ_{410} and γ_{670}, combined with a viscous lower mantle. On the one hand, once the slab folds toward the upper plate, the trench advances, and uplift occurs on the upper plate. On the other hand, the backward bend of the slab driven by trench retreat enhances an upper plate dynamic low. Episodic dynamic topographic highs and lows, as well as tilting toward and away from the trench, are promoted by slab folding.

Category 4 is characterized by a first phase, in which the slab deforms into the MTZ and shows a topographic evolution at the surface similar to the folding slab (category 3). The trench advance and retreat motion precedes the dynamic topographic variation in time. Yet the dynamic tilting of the upper plate toward and away from the trench depends on the slab folding behavior into the MTZ. Later, the slab sinks into the lower mantle (avalanche), and we observe an abrupt increase in trench velocity followed by an abrupt dynamic low and a tilt of the upper plate toward the trench. This surface fingerprint is similar to that observed for the flat slab (category 2). Hence, the slab surface expression for category 4 is a combination between the folding and flat slab cases (categories 3 and 2, respectively).

In agreement with Crameri & Lithgow-Bertelloni, (2017), we found that once the slab tip reaches the 670-km discontinuity, the mantle convection cell become much larger, leading to a tilt of the overriding plate. Under this condition, the dynamic topography of the overriding plate is reduced abruptly. When the slab is ponding in the MTZ, the dynamic topography remains low, indicating that the underlying mantle flow keeps on being dragged down from underneath the upper plate. Moreover, we see that folding-slab behavior leads to episodic changes in the slab morphology. Slabs may fold forward and backward, leading to episodic trench advance and retreat motions. Hence, the trench kinematics tunes the ability of the dynamic topography to go up and down. This finding agrees with previous studies (e.g., Cerpa et al., 2014; Guillaume et al., 2009; *Lee & King,* 2001), who show that slab dips vary in a time-dependent manner as soon as they encounter a strong barrier as the 670-km discontinuity inducing episodic changing in the trench velocity, and, in turn, building up topographic highs and lows close to the trench.

Our results show a key role of slab dynamics in controlling trench motion and the dynamic topography of the upper plate. However, previous studies have shown that trench motions may depend on 3D flow in the mantle (Funiciello et al., 2003; Funiciello et al., 2006; Schellart et al., 2007). In our study, the main controlling factors on the surface fingerprint are the lower mantle viscosity and mantle phase transitions of the olivine once the slab reaches the 670-km depth discontinuity, and our results can be thus considered valid in 3D settings if our 2D models are set at the center of a wide 3D slab. By contrast, narrower 3D models should increase the trench velocity and thus might change the dynamics of the slab at depth. Nonetheless, the dynamic topography should remain the same for a given set of slab category (direct sinking, flat slab, and folding slab). Further work is necessary to test this idea.

It has been known that the upper mantle deforms by dislocation creep (Hirth & Kohlstedt*,* 2003; Karato & Wu*,* 1993). Dislocation creep may lead to a lower viscosity into the asthenosphere, compared to the presented models, inducing a better decoupling between the plates and the mantle, which would be less

10.1029/2019JB017962

favorable to trench retreat (e.g.Billen & Arredondo, 2018, Capitanio et al., 2007). Additionally, in case of an upper mantle with a larger viscosity (>2.10^{20} Pa·s), a delay in fold formation at depth might be expected. Indeed, the size of the fold as well as the spacing between two successive folds may increase. Also, it would have an effect on the slab sinking velocity that may delay the timing of a fold formation into the upper mantle (e.g.Billen & Hirth, 2007, Čížková et al., 2007). Hence, the oscillation in the trench advance and retreat migration might be reduced. Similarly, an increase of viscosity of the upper mantle may be comparable to an increase in the strength and buoyancy of the subducting plate. Indeed, as we show for the oldest slab cases (Sections 3.5 and 3.6), the amplitude of the folds and the timing between two folds increase, while the trench velocity is reduced for youngest initial age (A_{plate}) of the subducting plate. Most importantly, an increase of upper mantle viscosity or the strength and buoyancy of the subducting plate delay the spacing between two uplift episodes and reduce the magnitude of the uplift of the upper plate. Hence, by changing those model characteristics (third dimension, upper mantle rheology, composite rheology, and weak layer viscosity), the presented category boundaries in Figure 3 would likely shift as consequence, but the characteristic surface fingerprints should remain similar for the corresponding slab category (i.e., flat, straight, and buckling slabs).

There is observational evidence for time-dependent variation surface fingerprints that may be linked to deep slab dynamics in the mantle MTZ. The surface expression of deep mantle dynamics has been explored and analyzed at global and local scale. At the global scale, the present day signal of deep subduction is well registered both in the geoid and topography (Flament et al., 2013; Forte et al., 1993; *Zhong et al.,* 1996), even if the fit between residual topography and dynamic topography is still low (Steinberger et al., 2001). Marine large-scale inundation has been interpreted as a signal of large-scale continental tilting due to deep subduction. Other examples come from continental subsidence of the Russian platform during the Devonian to Permian (Mitrovica et al., 1996) and the subsidence of the Karoo Basin during the Late Carboniferous to Early Triassic (Pysklywec & Mitrovica, 1999), both attributed to the subduction evolution and slab penetration into the lower mantle, leading to the subsidence of basins. In addition, the subsidence of the Australian plate might be attributed by a significant amount of slab material localized within the mantle MTZ (DiCaprio et al., 2009; Heine et al., 2010), which pulls down the continental plate.

Another test site for deep subduction is represented by the penetration of the Farallon slab under North America into the lower mantle, probably in the Late Cretaceous. The deep slab penetration has been suggested to generate subsidence of several hundreds of meters producing large-scale flooding (Gurnis, 1990; Gurnis et al., 2000; Liu et al., 2008; Mitrovica et al., 1996). Subsidence rates have been calibrated with the lower mantle viscosity providing a picture similar to what has been found in our model results.

The dynamic topography related to slab folding has not yet been described in nature. Deciphering alternating episodes of subsidence and uplift in the geological record is indeed more complicated. Our models show that the period of the expected signal is on the order of tens of millions of years but also that the vertical motion is accompanied by horizontal advance motion of the trench, as both will be dictated by the oscillation of the trench motion. We expect alternatively extensional or neutral tectonics regime and compression related to subsidence and uplift, respectively. One possible example is the compressional tectonic episodes and the variation of the arc volcanism as recognized in the Andes that has been commonly attributed to variations of the slab dip angle (Folguera et al., 2006; Kay et al., 2005). This work provides new insights to explain other alternating compressional/extensional patterns of deformation over mobile belts.

5. Conclusions

In this study, using a series of 2D, single-sided, self-consistent thermo-mechanical subduction models, we investigate how slab dynamics at depth may affect the surface topography of the upper plate. A systematic study shows that within a plausible range of the olivine phase transitions, mantle viscosity contrasts, and ages of subducting plates, there are many cases where the surface topography is strongly affected by the underlying slab dynamics. Cases where slabs sink straight into the deep mantle, which display a vertical morphology, induce a quasi-stationary trench state at the surface, as well as a relative flat long-wavelength topographic signal of the upper plate over time. The coexistence of a strong post-spinel transition (<-2 MPa/K) Clapeyron slope combined with a viscous lower mantle ($\geq 1.2 \times 10^{22}$ Pa·s) hampers, at least temporarily, slab penetration into the lower mantle and induces slabs to lay down horizontally in the MTZ, thereby driving trench retreat. As a result, a wide convection cell beneath the upper plate induces a dynamic low of the entire upper plate. Slab folding and buckling are typical for both strong Clapeyron slopes at 410 km depth and 670 km depth and are characterized by episodes of trenches retreat and advance motion. These specific kinematics lead to cyclic changes of the mantle flow below the upper plate and induce episodic variation of dynamic topography, by pulling up and down the upper plate according to the slab folding a depth. Changes in slab dynamics occur regularly throughout Earth history. The associated changes of the surface topography will help us constrain such deep slab behavior through time.

Acknowledgments
We thank the editor and two anonymous reviewers whose comments helped improving the manuscript. This work has received funding from the European Union's Horizon 2020 research and innovation programme under the Marie Skoldowska-Curie grant agreement No 674899. The grant to Department of Science, Roma Tre University (MIUR-Italy Dipartimenti di Eccellenza, ARTICOLO 1, COMMI 314-337 LEGGE 232/2016) is gratefully acknowledged. This work was funded by NERC (grants NE/J008028/1 and NE/M000281/1) and used the ARCHER UK National Supercomputing Service (http://www.archer.ac.uk). Supplementary Information accompanies this paper at https://doi.org/10.5281/zenodo.3574673

References

Agrusta, R., Goes, S., & van Hunen, J. (2017). Subducting-slab transition-zone interaction: Stagnation, penetration and mode switches. *Earth and Planetary Science Letters*, *464*, 10–23. https://doi.org/10.1016/j.epsl.2017.02.005

Agrusta, R., Van Hunen, J., & Goes, S. (2014). The effect of metastable pyroxene on the slab dynamics. *Geophysical Research Letters*, *41*(24), 8800–8808. https://doi.org/10.1002/2014GL062159

Agrusta, R., van Hunen, J., & Goes, S. (2018). Strong plates enhance mantle mixing in early Earth. *Nature Communications*, *9*(1), 2708. https://doi.org/10.1038/s41467-018-05194-5

Arnould, M., Coltice, N., Flament, N., Seigneur, V., & Müller, R. D. (2018). On the scales of dynamic topography in whole-mantle convection models. *Geochemistry, Geophysics, Geosystems*, *0*(0). https://doi.org/10.1029/2018GC007516

Běhounková, M., & Čížková, H. (2008). Long-wavelength character of subducted slabs in the lower mantle. *Earth and Planetary Science Letters*, *275*(1–2), 43–53. https://doi.org/10.1016/j.epsl.2008.07.059

Billen, M. I., & Arredondo, K. M. (2018). Decoupling of plate-asthenosphere motion caused by non-linear viscosity during slab folding in the transition zone. *Physics of the Earth and Planetary Interiors*, *281*, 17–30. https://doi.org/10.1016/j.pepi.2018.04.011

Billen, M. I., & Hirth, G. (2007). Rheologic controls on slab dynamics. *Geochemistry, Geophysics, Geosystems*, *8*, Q08012. https://doi.org/10.1029/2007GC001597

Capitanio, F., Morra, G., & Goes, S. (2007). Dynamic models of downgoing plate-buoyancy driven subduction: Subduction motions and energy dissipation. *Earth and Planetary Science Letters*, *262*(1–2), 284–297. https://doi.org/10.1016/j.epsl.2007.07.039

Cerpa, N. G., Araya, R., Gerbault, M., & Hassani, R. (2015). Relationship between slab dip and topography segmentation in an oblique subduction zone: Insights from numerical modeling. *Geophysical Research Letters*, *42*, 5786–5795. https://doi.org/10.1002/2015GL064047

Cerpa, N. G., Hassani, R., Gerbault, M., & Prévost, J. H. (2014). A fictitious domain method for lithosphere-asthenosphere interaction: Application to periodic slab folding in the upper mantle. *Geochemistry, Geophysics, Geosystems*, *15*, 1852–1877.

Christensen, U. R. (1996). The influence of trench migration on slab penetration into the lower mantle. *Earth and Planetary Science Letters*, *140*(1–4), 27–39. https://doi.org/10.1016/0012-821X(96)00023-4

Christensen, U. R., & Yuen, D. A. (1985). Layered convection induced by phase transitions. *Journal of Geophysical Research*, *90*(B12), 10291. https://doi.org/10.1029/JB090iB12p10291

Čížková, H., & Bina, C. R. (2013). Effects of mantle and subduction-interface rheologies on slab stagnation and trench rollback. *Earth and Planetary Science Letters*, *379*, 95–103. https://doi.org/10.1016/j.epsl.2013.08.011

Čížková, H., van den Berg, A. P., Spakman, W., & Matyska, C. (2012). The viscosity of Earth's lower mantle inferred from sinking speed of subducted lithosphere. *Physics of the Earth and Planetary Interiors*, *200–201*, 56–62. https://doi.org/https://doi.org/10.1016/j.pepi.2012.02.010

Čížková, H., van Hunen, J., & van den Berg, A. (2007). Stress distribution within subducting slabs and their deformation in the transition zone. *Physics of the Earth and Planetary Interiors*, *161*(3), 202–214. https://doi.org/https://doi.org/10.1016/j.pepi.2007.02.002

Crameri, F., & Lithgow-Bertelloni, C. (2017). Abrupt upper-plate tilting during slab-transition-zone collision. *Tectonophysics*. https://doi.org/10.1016/j.tecto.2017.09.013

Crameri, F., Schmeling, H., Golabek, G. J., Duretz, T., Orendt, R., Buiter, S. J. H., et al. (2012). A comparison of numerical surface topography calculations in geodynamic modelling: An evaluation of the "sticky air" method. *Geophysical Journal International*, *189*(1), 38–54. https://doi.org/10.1111/j.1365-246X.2012.05388.x

DiCaprio, L., Gurnis, M., & Müller, R. D. (2009). Long-wavelength tilting of the Australian continent since the Late Cretaceous. *Earth and Planetary Science Letters*, *278*(3), 175–185. https://doi.org/https://doi.org/10.1016/j.epsl.2008.11.030

Duretz, T., Gerya, T. V., & May, D. A. (2011). Numerical modelling of spontaneous slab breakoff and subsequent topographic response. *Tectonophysics*, *502*(1-2), 244–256.

Faccenda, M., & Dal Zilio, L. (2017). The role of solid–solid phase transitions in mantle convection. *Lithos*, *268–271*, 198–224. https://doi.org/10.1016/j.lithos.2016.11.007

Faccenna, C., Becker, T. W., Conrad, C. P., & Husson, L. (2013). Mountain building and mantle dynamics, 32(December 2012). https://doi.org/10.1029/2012TC003176

Flament, N., Gurnis, M., & Muller, R. D. (2013). A review of observations and models of dynamic topography. *Lithosphere*, *5*(2), 189–210. https://doi.org/10.1130/L245.1

Folguera, A., Zapata, T., & Ramos, V. A. (2006). Late Cenozoic extension and the evolution of the Neuquén Andes. *SPECIAL PAPERS-GEOLOGICAL SOCIETY OF AMERICA*, *407*, 267.

Forte, A. M., Mitrovica, J. X., & Espesset, A. (2002). Geodynamic and seismic constraints on the thermochemical structure and dynamics of convection in the deep mantle. *Philosophical Transactions. Series A, Mathematical, Physical, and Engineering Sciences*, *360*(1800), 2521–2543. https://doi.org/10.1098/rsta.2002.1079

Forte, A. M., Peltier, W. R., Dziewonski, A. M., & Woodward, R. L. (1993). Dynamic surface topography: A new interpretation based upon mantle flow models derived from seismic tomography. *Geophysical Research Letters*, *20*(3), 225–228. https://doi.org/10.1029/93GL00249

Fukao, Y., & Obayashi, M. (2013). Subducted slabs stagnant above, penetrating through, and trapped below the 660 km discontinuity. *Journal of Geophysical Research: Solid Earth*, *118*, 5920–5938. https://doi.org/10.1002/2013JB010466

Funiciello, F., Faccenna, C., Giardini, D., & Regenauer-Lieb, K. (2003). Dynamics of retreating slabs: 2. Insights from three-dimensional laboratory experiments. *Journal of Geophysical Research*, *108*, 2207. https://doi.org/10.1029/2001JB000896

Funiciello, F., Moroni, M., Piromallo, C., Faccenna, C., Cenedese, A., & Bui, H. A. (2006). Mapping mantle flow during retreating subduction: Laboratory models analyzed by feature tracking. *Journal of Geophysical Research*, *111*, B03402. https://doi.org/10.1029/2005JB003792

Garel, F., Goes, S., Davies, D. R., Davies, J. H., Kramer, S. C., & Wilson, C. R. (2014). Interaction of subducted slabs with the mantle transition-zone: A regime diagram from 2-D thermo-mechanical models with a mobile trench and an overriding plate. *Geochemistry, Geophysics, Geosystems*, *15*, 1739–1765. https://doi.org/10.1002/2014GC005257

Goes, S., Agrusta, R., van Hunen, J., & Garel, F. (2017). Subduction-transition zone interaction: A review. *Geosphere*, *13*(3), 644–664. https://doi.org/10.1130/GES01476.1

Guillaume, B., Martinod, J., & Espurt, N. (2009). Variations of slab dip and overriding plate tectonics during subduction: Insights from analogue modelling. *Tectonophysics*, *463*(1– 4), 167–174. https://doi.org/10.1016/j.tecto.2008.09.043

Gurnis, M. (1990). Bounds on global dynamic topography from phanerozoic flooding of continental platforms. *Nature*. https://doi.org/10.1038/344754a0

Gurnis, M., Mitrovica, J. X., Ritsema, J., & Van Heijst, H. J. (2000). Constraining mantle density structure using geological evidence of surface uplift rates: The case of the African Superplume. *Geochemistry, Geophysics, Geosystems*, *1*(7). https://doi.org/10.1029/1999GC000035

Hager, B. H. (1984). Subducted slabs and the geoid: constraints on mantle rheology and flow. *Journal of Geophysical Research*, *89*(B7), 6003–6015. https://doi.org/10.1029/JB089iB07p06003

Hager, B. H., & Richards, M. A. (1989). Long-wavelength variations in Earth's geoid: Physical models and dynamical implications. *Philosophical Transactions of the Royal Society A: Mathematical, Physical and Engineering Sciences*, *328*(1599), 309–327. https://doi.org/10.1098/rsta.1989.0038

Heine, C., Müller, R. D., Steinberger, B., & DiCaprio, L. (2010). Integrating deep Earth dynamics in paleogeographic reconstructions of Australia. *Tectonophysics*, *483*(1–2), 135–150. https://doi.org/10.1016/j.tecto.2009.08.028

Hirth, G., & Kohlstedt, D. L. (2003). Rheology of the upper mantle and the mantle wedge: A view from the experimentalists upper mantle. We first analyze experimental data to provide a critical review of flow. *Geophysical Monograph Series*, *138*, 83–105. https://doi.org/10.1029/138GM06

Husson, L., & Ricard, Y. (2004). Stress balance above subduction: Application to the Andes. *Earth and Planetary Science Letters*, *222*(3–4), 1037–1050. https://doi.org/10.1016/j.epsl.2004.03.041

Kaban, M. K., Schwintzer, P., & Reigber, C. (2004). A new isostatic model of the lithosphere and gravity field. *Journal of Geodesy*, *78*(6), 368–385. https://doi.org/10.1007/s00190-004-0401-6

Karato, S., & Wu, P. (1993). Rheology of the upper mantle: A synthesis. *Science*, *260*(5109), 771 LP–778. https://doi.org/10.1126/science.260.5109.771

Katsura, T., & Ito, E. (1989). The system Mg_2SiO_4-Fe_2SiO_4 at high pressures and temperatures: Precise determination of stabilities of olivine, modified spinel, and spinel. *Journal of Geophysical Research*, *94*(B11), 15,663–15,670. https://doi.org/10.1029/JB094iB11p15663

Kay, S. M., Godoy, E., & Kurtz, A. (2005). Episodic arc migration, crustal thickening, subduction erosion, and magmatism in the south-central Andes. *Geological Society of America Bulletin*, *117*(1–2), 67–88.

Kincaid, C., & Olson, P. (1987). An experimental study of subduction and slab migration. *Journal of Geophysical Research*, *92*(B13), 13,832–13,840. https://doi.org/10.1029/JB092iB13p13832

Lee, C., & King, S. D. (2011). Dynamic buckling of subducting slabs reconciles geological and geophysical observations. *Earth and Planetary Science Letters*, *312*(3–4), 360–370. https://doi.org/10.1016/j.epsl.2011.10.033

Litasov, K. D., & Ohtani, E. (2007). Effect of water on the phase relations in Earth's mantle and deep water cycle, *Special Papers-Geological Society of America 2421*(08), 115–156. https://doi.org/10.1130/2007.2421(08)

Lithgow-Bertelloni, C. (1997). Cenozoic subsidence and uplift of continents from time-varying dynamic topography. *Geology*, *25*(8), 735–738. https://doi.org/10.1130/0091-7613(1997)025<0735:CSAUOC>2.3.CO;2

Lithgow-Bertelloni, C., & Silver, P. (1998). Dynamic topography, plate driving forces and the African superswell. *Nature*, *395*(September), 345–348. https://doi.org/10.1038/26212

Liu, L., & Gurnis, M. (2010). Dynamic subsidence and uplift of the Colorado Plateau. *Geology*, *38*(7), 663–666.

Liu, L., Spasojevic, S., & Gurnis, M. (2008). Reconstructing Farallon plate subduction beneath North America Back to the Late Cretaceous. *Science*, *322*(5903), 934–938. https://doi.org/10.1126/science.1162921

Mao, W., & Zhong, S. (2018). Slab stagnation due to a reduced viscosity layer beneath the mantle transition zone. *Nature Geoscience*, 41–43. https://doi.org/10.1038/s41561-018-0225-2

Martinod, J., Regard, V., Letourmy, Y., Henry, H., Hassani, R., Baratchart, S., & Carretier, S. (2016). How do subduction processes contribute to forearc Andean uplift? Insights from numerical models. *Journal of Geodynamics*, *96*, 6–18.

Mitrovica, J. X., Beaumont, C., & Jarvis, G. T. (1989). Tilting of continental interiors by the dynamical effects of subduction. *Tectonics*, *8*(5), 1079–1094. https://doi.org/10.1029/TC008i005p01079

Mitrovica, J. X., Pysklywec, R. N., Beaumont, C., & Rutty, A. (1996). The Devonian to Permian sedimentation of the Russian Platform: An example of subduction controlled long-wavelength tilting of continents. *J. Geodyn.*, *22*(112), 79–96. https://doi.org/10.1016/0264-3707(96)00008-7

Moresi, L., & Gumis, M. (1996). Dynamic Flow Models. *Earth and Planetary Science Letters*, *38*(95), 15–28.

Panasyuk, S. V., & Hager, B. H. (2000). Models of isostatic and dynamic topography, geoid anomalies, and their uncertainties. *Journal of Geophysical Research*, *105*(B12), 28,199–28,209.

Pérez-Peña, J. V., Azor, A., Azañón, J. M., & Keller, E. A. (2010). Active tectonics in the Sierra Nevada (Betic Cordillera, SE Spain): Insights from geomorphic indexes and drainage pattern analysis. *Geomorphology*, *119*(1), 74–87. https://doi.org/https://doi.org/10.1016/j.geomorph.2010.02.020

Pysklywec, R. N., & Mitrovica, J. X. (1999). The role of subduction-induced subsidence in the evolution of the Karoo Basin. *The Journal of Geology*, *107*(2), 155–164. https://doi.org/10.1086/314338

Ricard, Y., Richards, M., Lithgow-Bertelloni, C., & Le Stunff, Y. (1993). A geodynamic model of mantle density heterogeneity. *Journal of Geophysical Research*, *98*(B12), 21,895–21,909. https://doi.org/10.1029/93JB02216

Schellart, W. P., Freeman, J., Stegman, D. R., Moresi, L., & May, D. (2007). Evolution and diversity of subduction zones controlled by slab width. *Nature*, *446*(7133), 308–311. https://doi.org/10.1038/nature05615

Sembroni, A., Molin, P., Pazzaglia, F. J., Faccenna, C., & Abebe, B. (2016). Evolution of continental-scale drainage in response to mantle dynamics and surface processes: An example from the Ethiopian Highlands. *Geomorphology*, *261*, 12–29. https://doi.org/10.1016/j.geomorph.2016.02.022

Sigloch, K., & Mihalynuk, M. G. (2013). Intra-oceanic subduction shaped the assembly of Cordilleran North America. *Nature*, *496*(7443), 50–56. https://doi.org/10.1038/nature12019

Steinberger, B., Schmeling, H., & Marquart, G. (2001). Large-scale lithospheric stress field and topography induced by global mantle circulation. *Earth and Planetary Science Letters*, *186*(1), 75–91. https://doi.org/https://doi.org/10.1016/S0012-821X(01)00229-1

Tosi, N., Maierová, P., & Yuen, D. A. (2015). Influence of variable thermal expansivity and conductivity on deep subduction. *Subduction Dynamics*. https://doi.org/doi:10.1002/9781118888865.ch6

Tosi, N., Yuen, D. A., de Koker, N., & Wentzcovitch, R. M. (2013). Mantle dynamics with pressure- and temperature-dependent thermal expansivity and conductivity. *Physics of the Earth and Planetary Interiors*, *217*, 48–58. https://doi.org/10.1016/j.pepi.2013.02.004

Turcotte, D. L., & Schubert, G. (2002). *Geodynamics* (2nd ed., 456 pp.).

Van Der Meer, D. G., Spakman, W., Van Hinsbergen, D. J. J., Amaru, M. L., & Torsvik, T. H. (2010). Towards absolute plate motions constrained by lower-mantle slab remnants. *Nature Geoscience*, *3*(1), 36–40. https://doi.org/10.1038/ngeo708

Wang, H., Agrusta, R., & van Hunen, J. (2015). Advantages of a conservative velocity interpolation (CVI) scheme for particle-in-cell methods with application in geodynamic modeling. *Geochemistry, Geophysics, Geosystems*, *16*, 2015–2023. https://doi.org/10.1002/2015GC005824

Watts, A. B. (1978). An analysis of isostasy in the world's oceans 1. Hawaiian-Emperor Seamount Chain. *Journal of Geophysical Research*, *83*(B12), 5989–6004. https://doi.org/10.1029/JB083iB12p05989

Xu, W., Lithgow-Bertelloni, C., Stixrude, L., & Ritsema, J. (2008). The effect of bulk composition and temperature on mantle seismic structure. *Earth and Planetary Science Letters*, *275*(1–2), 70–79. https://doi.org/10.1016/j.epsl.2008.08.012

Gerya, T. V, & Yuen, D. A. (2003). Characteristics-based marker-in-cell method with conservative finite-differences schemes for modeling geological flows with strongly variable transport properties. *Physics of the Earth and Planetary Interiors*, *140*(4), 293–318. https://doi.org/https://doi.org/10.1016/j.pepi.2003.09.006

Zhong, S., & Gurnis, M. (1994). Controls on trench topography from dynamic models of subducted slabs. *Journal of Geophysical Research*, *99*(B8), 15683. https://doi.org/10.1029/94JB00809

Zhong, S., Gurnis, M., & Hulbert, G. (1993). Accurate determination of surface normal stress in viscous flow from a consistent boundary flux method. *Physics of the Earth and Planetary Interiors*, *78*(1–2), 1–8. https://doi.org/10.1016/0031-9201(93)90078-N

Zhong, S. J., Gurnis, M., & Moresi, L. (1996). Free-surface formulation of mantle convection.1. Basic theory and application to plumes. *Geophysical Journal International*, *127*(3), 708–718. https://doi.org/10.1111/j.1365-246X.1996.tb04049